

# Co-VeGAN: Complex-Valued Generative Adversarial Network for Compressive Sensing MR Image Reconstruction

Bhavya Vasudeva<sup>1\*</sup><sup>1</sup>Dept. of ECE, IIT Roorkee, IndiaPuneesh Deora<sup>1\*</sup>Saumik Bhattacharya<sup>2</sup>Pyari Mohan Pradhan<sup>1</sup><sup>2</sup>Dept. of E&ECE, IIT Kharagpur, India

## Abstract

*Compressive sensing (CS) is widely used to reduce the image acquisition time of magnetic resonance imaging (MRI). Though CS-based undersampling has numerous benefits, like high-quality images with fewer motion artefacts and low storage requirement, the reconstruction of the image from the CS undersampled data is an ill-posed inverse problem which requires extensive computation and resources. In this paper, we propose a novel deep network that can process complex-valued input to perform high-quality reconstruction. Our model is based on a complex-valued generative adversarial network (Co-VeGAN) that uses residual-in-residual dense blocks in a novel dense U-net generator with patch-based discriminator. We introduce a wavelet-based loss in the complex GAN model for better reconstruction quality. Further, a novel activation function is proposed for complex-valued entities, which is not only sensitive to the variations in their phase but also has a learnable profile. We have presented detailed analyses of different network settings as well as various activation functions to support our contributions. Extensive evaluation of the proposed approach on different datasets and sampling masks demonstrate that the proposed model significantly outperforms the existing CS-MRI reconstruction techniques in terms of peak signal-to-noise ratio as well as structural similarity index.*

## 1. Introduction

Magnetic resonance imaging (MRI) is a frequently used medical imaging modality in clinical practice as it proves to be an excellent non-invasive source for revealing structural as well as anatomical information. A major shortcoming of the MRI acquisition process is its considerably long scan time. This is due to sequential acquisition of large volumes of data, not in the image domain but in  $k$ -space, i.e. Fourier domain. Such a prolonged scanning time can cause significant artefacts because of physiological motion, movement

of patient during the scan. It may also hinder the use of MRI in time-critical diagnosis. A possible way to speed-up the imaging process is by parallel imaging techniques [33], [14]. However, the number and arrangement of the receiver coils drastically impact the acceleration factor for such techniques, and could possibly introduce imaging artefacts. Another possible way for fast acquisition is leveraging compressive sensing (CS) [11] theory based undersampling, which is used very often for this purpose. However, doing this renders the inverse problem ill-posed, making the recovery of high-quality MR images extremely challenging. Moreover, the presence of noise during the acquisition may also impact the reconstruction quality.

Conventional approaches for CS-MRI reconstruction focus extensively on the usage of sparse representations to assume prior knowledge on the structure of the MR image to be reconstructed. Sparse representations can be explored by the use of predefined transforms [28] such as total variation, discrete wavelet transform, discrete Fourier transform, discrete cosine transform, etc. Alternatively, dictionary learning based methods [35] learn sparse representations from the subspace spanned by the data. Both these types of approaches suffer from long computation time due to the iterative nature of the optimization processes. Moreover, the universally applicable sparsifying transforms might find it difficult to completely capture the fine details as observed in biological tissues [27].

Deep learning frameworks have enjoyed great success in similar inverse problems such as single-image super resolution [10], denoising [44], etc., where the methods try to recover missing information from incomplete or noisy data. Yang *et al.* [46] used the alternating direction method of multipliers (ADMM) algorithm [6] to train their deep network for CS-MRI reconstruction. With the recent advancements of generative adversarial networks (GANs) [13, 22], CS-MRI reconstruction problems are also addressed using adversarial learning framework. In a recent study, Bora *et al.* [5] have shown that pretrained generative models like variational autoencoders and GANs [13] can be used for recovery of CS signal without making use of sparsity at all. Yang *et al.* [45] have proposed a U-net [37] based generator,

---

\*equal contribution

following a refinement learning based approach, with mean squared error (MSE) and perceptual loss to reconstruct the images. The authors of [34] have proposed a fully residual network using addition-based skip connections. They used cyclic loss for data consistency constraints in the training process to achieve better reconstruction quality. Deora *et al.* [9] have proposed a U-net based generator with a patch-based discriminator [22] to perform the reconstruction task. Along with mean absolute error (MAE) and structural similarity (SSIM) [47], authors used Wasserstein loss [2] to improve the adversarial learning. The complex-valued data is split and concatenated as two real-valued channels. Hammernick *et al.* [16] follow a similar approach to split the complex-valued data, and train a variational network, where they learn separate filters for real and imaginary data. Marandani *et al.* [29] have introduced affine projection operator in-between the generator and the discriminator to improve the data consistency in the reconstructed images.

Although deep adversarial networks have significantly improved the quality of the CS-MRI reconstruction, one of the biggest short-comings is that they work on real-valued inputs even though the input is inherently complex-valued. The other limitation is that almost all reconstruction networks depend on pixel-wise  $l_2$  or  $l_1$  losses. This efficiently reconstructs the low-frequency components of data, but often fails to generate the mid and high-frequency information which depicts fine textural and structural parts of an image [20].

**Motivation of the work:** Complex parameter space provides several benefits over real parameter space. Apart from having biological inspiration and significance [36], complex-valued representation not only increases the representational capacity of the network, it can be more stable than real-valued space in various applications [39, 8]. Complex-valued operations can be performed with easy optimization techniques [31] without sacrificing the generalization ability of the network [18]. Several researchers have reported that the complex-valued neural network exhibits faster learning with better robustness to noise [8, 3, 43]. Complex-valued operations also preserve the phase information which encodes fine structural details of an image [32, 39]. The importance of phase in images in terms of recovery of magnitude information has been discussed in [32]. A more mathematical motivation for the use of complex weights in convolutional neural networks is presented in [7]. Even with these striking benefits, complex-valued deep networks are not widely explored. Although some previous works have explored the use of complex representations in vision related tasks [39], [48], parallel MR imaging [41], MRI fingerprinting [40], audio-related tasks [39], the complex-valued GAN (Co-VeGAN) model has never been explored for any reconstruction problem, to the best of our knowledge.

**Contributions:** Complex-valued operations are widely unexplored for GAN architecture, and a Co-VeGAN model has never been explored for CS-MRI reconstruction problem. This work not only exploits complex-valued operations to achieve better reconstruction, but also documents the stability and quality of a Co-VeGAN based approach for a reconstruction problem with various loss functions and network settings. As complex-valued activation functions are a crucial part of complex-valued deep networks, we not only present a detailed evaluation of several existing activation functions, but also propose a novel complex-valued activation function that enhances the performance of the Co-VeGAN framework. The proposed activation has been formulated as a learnable (and flexible) function which is sensitive to the variations in the phase of the input. Further, in order to enhance the reconstruction quality, we propose a novel U-net based generator architecture by incorporating dense connections within the contracting and expanding paths to allow feature reuse between layers and improve the information flow. In addition, we introduce a novel Gaussian-weighted variant of wavelet loss in our model. As the  $\ell_1$  loss focuses on the low-frequency details, while the SSIM takes care of the high-frequency content in the reconstructed image, this loss function has been formulated to achieve better reconstruction of mid-frequency components of the MR image. To the best of our knowledge, wavelet loss has not been integrated with any complex-valued deep network before.

## 2. Methodology

The acquisition model of CS-MRI can be described as follows:

$$\mathbf{y} = \Phi \mathbf{x} + \zeta = \mathbf{U} \mathbf{F} \mathbf{x} + \zeta, \quad (1)$$

where  $\mathbf{x} \in \mathbb{R}^{K^2}$  is the desired image in vector form,  $\mathbf{y} \in \mathbb{C}^M$  denotes the observed data vector, the vector  $\zeta \in \mathbb{C}^M$  captures the noise.  $\mathbf{F} \in \mathbb{C}^{K^2 \times K^2}$  denotes the matrix to compute the 2D Fourier transform,  $\mathbf{U} \in \mathbb{R}^{M \times K^2}$  describes the matrix for undersampling. Given an observation  $\mathbf{y}$ , the aim of reconstruction is to recover  $\mathbf{x}$  in the presence of a non-zero noise vector  $\zeta$ . We attempt the recovery of  $\mathbf{x}$  by using a GAN model.

### 2.1. Complex-valued GAN

A GAN comprises of two networks, namely a generator and a discriminator. In order to generate images which are similar to the samples of the distribution of true data  $\mathbf{y}_t$ , the generator  $G$  attempts to map an input vector  $\mathbf{z}$  to the output  $G(\mathbf{z})$ . On the other hand, the aim of the discriminator  $D$  is to classify the generated samples  $G(\mathbf{z})$  and the samples from the distribution of  $\mathbf{y}_t$ .

We propose the use of a complex-valued GAN which consists of a complex-valued  $G : \mathbb{C}^{K \times K} \rightarrow \mathbb{R}^{K \times K}$ , and a

real-valued  $D : \mathbb{R}^{K \times K} \rightarrow \mathbb{R}^{1 \times 1}$ . Although both  $G$  and  $D$  can be complex-valued, we opt for the use of a real-valued discriminator because both the generated and ground truth (GT) images are real-valued.

## 2.2. Complex-valued operations

In this section, we discuss the important operations required for the implementation of a complex-valued network, namely convolution, backpropagation, batch normalization (BN) [21], and activation.

### 2.2.1 Convolution

The complex-valued equivalent of real-valued 2D convolution is discussed below. The convolution of a complex-valued kernel  $\mathbf{W} = \mathbf{W}_R + i\mathbf{W}_I$  with complex-valued feature maps  $\mathbf{F} = \mathbf{F}_R + i\mathbf{F}_I$ , can be represented as  $\mathbf{A} = \mathbf{W} * \mathbf{F} = \mathbf{A}_R + i\mathbf{A}_I$ , where  $*$  denotes convolution operation,  $i$  denotes  $\sqrt{-1}$ , and

$$\begin{aligned}\mathbf{A}_R &= \mathbf{W}_R * \mathbf{F}_R - \mathbf{W}_I * \mathbf{F}_I, \\ \mathbf{A}_I &= \mathbf{W}_R * \mathbf{F}_I + \mathbf{W}_I * \mathbf{F}_R,\end{aligned}\quad (2)$$

similar to complex multiplication. In these notations, the subscripts **R** and **I** denote the real and imaginary parts of the complex-valued entities, respectively. In order to implement the aforementioned complex-valued convolution, we make use of real-valued tensors, where  $\mathbf{W}$  ( $\mathbf{F}$ ) is stored such that the imaginary part  $\mathbf{W}_I$  ( $\mathbf{F}_I$ ) is concatenated to the real part  $\mathbf{W}_R$  ( $\mathbf{F}_R$ ). The resultant includes four real-valued 2D convolutions as defined in (2), which is stored in a similar manner by concatenating  $\mathbf{A}_I$  to  $\mathbf{A}_R$ .

### 2.2.2 Backpropagation

Backpropagation can be performed on a function  $f$  that is non-holomorphic as long as it is differentiable with respect to its real and imaginary parts [25]. Since all the loss functions considered in this work are real-valued, we consider  $f$  to be a real-valued function of  $l$ -dimensional weight vector  $\mathbf{w}$ . The update rule of  $\mathbf{w}$  using gradient descent is written as:

$$\mathbf{w} = \mathbf{w} - \rho \nabla_{\bar{\mathbf{w}}} f(\mathbf{w}), \quad (3)$$

where  $\rho$  is the learning rate (LR),  $\bar{\mathbf{w}}$  denotes the complex conjugate, and the gradient of  $f$  is calculated as:

$$\begin{aligned}\nabla_{\bar{\mathbf{w}}} f(\mathbf{w}) &= \left[ \frac{\partial f}{\partial \bar{w}_1} \dots \frac{\partial f}{\partial \bar{w}_l} \right]^T \\ \frac{\partial f}{\partial \bar{w}} &= \frac{1}{2} \left( \frac{\partial f}{\partial w_R} + i \frac{\partial f}{\partial w_I} \right).\end{aligned}\quad (4)$$

### 2.2.3 Batch Normalization

We make use of the complex BN (CBN) applicable to complex numbers, proposed in [39]. To ensure that the complex

data is scaled in such a way that the distribution of real and imaginary components is circular, the 2D complex vector can be whitened as shown below:

$$\mathbf{x}_{std} = \mathbf{B}^{-\frac{1}{2}} (\mathbf{x} - \mathbb{E}[\mathbf{x}]), \quad (5)$$

where  $\mathbf{B}$  denotes the covariance matrix, and  $\mathbb{E}$  denotes expectation operator.  $\mathbf{B}$  can be represented as:

$$\mathbf{B} = \begin{bmatrix} \text{Cov}(\mathbf{x}_R, \mathbf{x}_R) & \text{Cov}(\mathbf{x}_R, \mathbf{x}_I) \\ \text{Cov}(\mathbf{x}_I, \mathbf{x}_R) & \text{Cov}(\mathbf{x}_I, \mathbf{x}_I) \end{bmatrix}. \quad (6)$$

Learnable parameters  $\gamma, \beta$  are used to scale and shift the aforementioned standardized vector as follows:

$$\mathbf{x}_{BN} = \gamma \mathbf{x}_{std} + \beta, \quad (7)$$

where  $\gamma$  is a  $2 \times 2$  matrix, and  $\beta$  is a complex number.

### 2.2.4 Activation

In order to work with complex-valued entities, several activation functions have been proposed in previous works [3]. One common class of complex activation functions is obtained when the same nonlinearity is applied separately on the real and imaginary parts. The complex equivalent of the commonly used rectified linear unit (CReLU) is given by:

$$\mathbb{CReLU}(a) = \text{ReLU}(a_R) + i\text{ReLU}(a_I), \quad (8)$$

where  $a$  is a complex-valued input. Similarly, the expression for the complex equivalent of parametric ReLU [17] (CPReLU) is formulated as follows:

$$\mathbb{CPReLU}(a) = \begin{cases} a_R + ia_I & 0 \leq a_R, 0 \leq a_I, \\ \beta_R a_R + ia_I & a_R < 0, 0 \leq a_I, \\ a_R + i\beta_I a_I & 0 \leq a_R, a_I < 0, \\ \beta_R a_R + i\beta_I a_I & a_R < 0, a_I < 0, \end{cases}$$

where  $\beta_R$  and  $\beta_I$  are trainable parameters. In this way, the complex equivalent of any activation function which works well for real-valued networks can be explored for complex-valued networks.

There is another class of complex activation functions where the nonlinearity is applied on the magnitude  $|a|$  and phase  $\angle a$  of  $a$ . One such activation is  $z$ ReLU [15], which allows a complex element to pass only if it lies in the first quadrant. It is given by:

$$zReLU(a) = \begin{cases} a & 0 \leq \angle a \leq \frac{\pi}{2}, \\ 0 & \text{otherwise.} \end{cases} \quad (9)$$

However, all the aforementioned activation functions are weakly sensitive to the changes in the phase of the input, which is not only important from the biological perspective

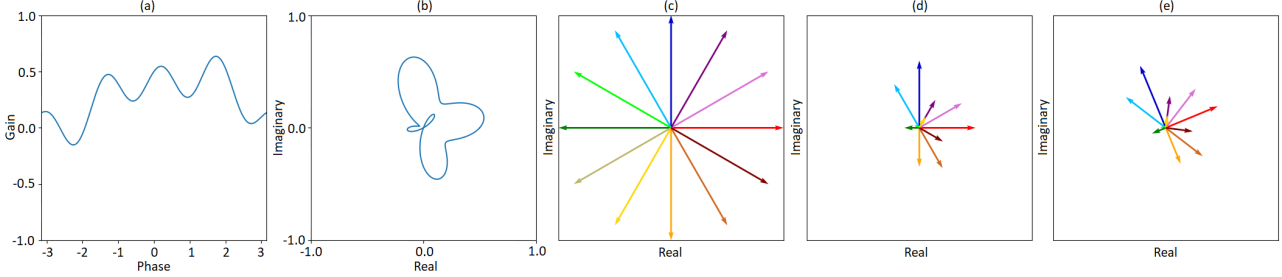


Figure 1. An example of PC-SoS, with the set of values:  $[w_0, w_1, w_2, \theta_0, \theta_1, \theta_2] = [0.08, -0.04, 0.06, 0.6, 0.4, 0.2]$ . (a) Plot of gain vs input phase, (b) plot of gain in complex space, (c) a set of complex inputs, (d) outputs of PC-SoS using gain shown in (a) with  $\phi = 0$ , and (e) outputs with  $\phi = \frac{\pi}{8}$ .

but also crucial for the complex representation. Virtue *et al.* [40] have proposed the cardioid activation, where the input phase is preserved at the output, and the magnitude of the output is sensitive to the phase of the input. It is formulated as:

$$\text{Cardioid}(a) = g(\angle a)a = \frac{1}{2}(1 + \cos(\angle a))a, \quad (10)$$

where  $g(\cdot)$  denotes the gain, which is positive-valued for phase preservation.

However, phase preservation reduces the flexibility of the activation function because change in the phase from the input to the output can be viewed as the delay of a neuron. Moreover, since the phase is modified at the CBN layer, its preservation at the activation layer might not prove useful. Another drawback of cardioid is that the gain is fixed, and its shape is not learnable. Due to its fixed shape, it favours positive real-valued inputs over negative ones, as  $g(0) = 1$  and  $g(\pi) = 0$ . Also, it is designed to favour real-valued inputs over purely imaginary inputs, as  $g(\frac{\pi}{2}) = 0.5$ , without much intuition.

We propose a novel activation function, where each neuron can introduce a phase change (PC)  $\phi$  in the input. This can also be viewed as allowing coupling between  $a_R$  and  $a_I$ . Further, in order to allow the magnitude of the output to be sensitive to the phase of the input, any continuous function of the input phase can be used as the gain. Also, this function should be periodic with period  $2\pi$ , so that it is continuous for all values of the phase. We propose the use of a weighted sum of sinusoids (SoS) in this work, to provide flexibility and maintain periodicity. The proposed PC-SoS is formulated as follows:

$$PC\text{-}SoS(a) = \frac{\sum_{p=0}^{P_S-1} w_p \{1 + \cos(2^p(\angle a - \theta_p))\}}{2 \sum_{p=0}^{P_S-1} |w_p| + \epsilon} ae^{i\phi}, \quad (11)$$

where  $w_p$ ,  $\theta_p$  and  $\phi$  are trainable parameters,  $P_S$  denotes the number of sinusoids taken, and  $\epsilon$  is a small constant to

avoid division by 0. The use of trainable parameters  $w_p$  and  $\theta_p$  allow the framework to learn suitable gain functions. The number of extra parameters introduced by PC-SoS is very small as compared to the total number of weights already present in the framework, since for a particular channel of a layer, the activation shares its weights. The numerator is normalized by the sum of the absolute value of the weights, so that the gain remains bounded in  $[-1, 1]$ , to avoid the problem of exploding gradient. As the gain can take negative values, the phase may not be preserved. In order to control the trade-off between the flexibility and the increase in the number of trainable parameters,  $P_S$  is set as 3 in this study. Fig. 1 illustrates an example of PC-SoS. It is evident that PC-SoS has a very flexible learnable shape, and that it can cause changes in the phase of the complex inputs.

In order to demonstrate the importance of allowing negative gain and using  $\phi$  in PC-SoS, we consider two of its variants. In the first case,  $\phi$  is set as 0 and absolute value of weights is taken in the numerator as well, so that the gain is bounded in  $[0, 1]$ . This is the phase preserving equivalent (PP) of PC-SoS, and is named as PP-SoS. When  $w_0 = 1$  and the rest of the parameters are set as 0, PP-SoS is reduced to cardioid. In order to highlight the importance of  $\phi$ , we consider another variant, where negative gain is allowed, as in (11), but  $\phi$  is set as 0. In this case, the negative gain may change the phase, but the value of  $\tan^{-1}(\frac{a_I}{a_R})$  remains the same at the output. Thus, this tangent inverse preserving (TIP) equivalent of PC-SoS is named as TIP-SoS.

### 2.3. Network Architecture

The generator architecture used in the proposed framework is shown in Fig. 2(a). It is based on a U-net architecture. The left side is a contracting path, where each step involves the creation of downsampled feature maps using a convolutional layer with stride 2, which is followed by CBN and activation function. The right side is an expanding path, where each step consists of upsampling (by a factor of two), convolutional layer to create new feature maps, followed by CBN and activation layers. In order to provide richer context about the low-level features for su-

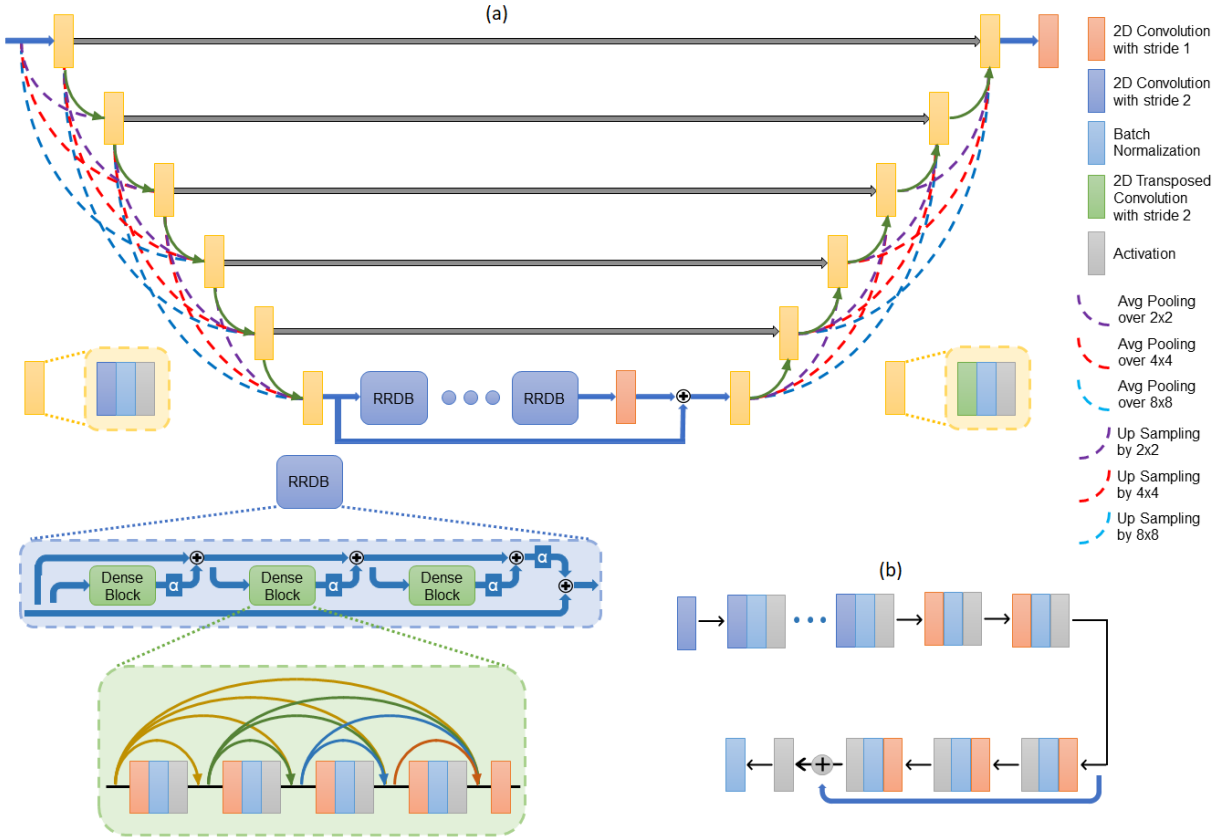


Figure 2. (a) Proposed dense U-net generator architecture with RRDBs and (b) discriminator architecture.

terior reconstruction, the low-level feature maps from the contracting path are concatenated to the high-level feature maps of same size in the expanding path.

In this work, the use of dense connections between the steps (layers) within the contracting as well as the expanding path has been proposed. These dense connections [19] help to improve the flow of information between the layers and encourage the features from the preceding layers to be reused. There is also an added benefit of increase in variation of available information by concatenation of feature maps. Since the feature maps at various layers are not of the same size, average pooling and upsampling (with bilinear interpolation) operations have been introduced in the dense connections between the layers of the contracting path and the expanding path, respectively. However, the use of these operations to change the size of the feature maps by a factor greater than  $r$  (less than size  $\frac{K}{2^r} \times \frac{K}{2^r}$ ) not only increases the computational and memory requirement, but also reduces the quality of information available to the subsequent layers. As shown in Fig. 2(a),  $r$  is set as 3 in this work.

Further, residual-in-residual dense blocks (RRDBs) [42] are incorporated at the lowest layer of the generator, where feature maps of size  $\frac{K}{32} \times \frac{K}{32}$  are present. Each block uses

residual learning across each dense block, as well as across a group of three dense blocks. At both the levels, residual scaling is used, i.e. the residuals are scaled by  $\alpha$  before they are added to the identity mapping, as shown in Fig. 2(a). These RRDBs not only make the network length variable, because of the residual connections which make identity mappings easier to learn, but also make a rich amount of information accessible to the deeper layers, through the dense connections. They also help to overcome the problem of vanishing gradients at the shallower layers.

At the output of the generator, a hyperbolic tangent activation is applied, which brings the real as well as imaginary parts of the final feature map in the range  $[-1, 1]$ . These are then brought to the range  $[0, 1]$ . In order to make the output real-valued, the absolute value is obtained (which lies in the range  $[0, \sqrt{2}]$ ), and then brought back to the range  $[-1, 1]$ .

The discriminator architecture is based on a standard convolutional neural network, as shown in Fig. 2(b). It has 11 convolutional layers, each of which is followed by BN and leaky ReLU activation function. We use a patch-based discriminator to increase the focus on the reconstruction of high-frequency content. The patch-based discriminator scores each patch of the input image separately, and

its output is the mean of the individual patch scores. This framework makes the network insensitive to the input size.

## 2.4. Training Losses

### 2.4.1 Adversarial Loss

In order to constrain the generator to produce the MR image corresponding to the samples acquired in the  $k$ -space, it is conditioned [30] over the zero-filled reconstruction (ZFR) given by:

$$\mathbf{x}_u = \Phi^H \mathbf{y} = \mathbf{F}^H \mathbf{U}^H \mathbf{y}, \quad (12)$$

where  $\mathbf{x}_u \in \mathbb{C}^{K^2}$ ,  $H$  denotes the Hermitian operator. Conventionally, the solution to the minmax game between the generator and the discriminator is obtained by using binary cross-entropy based loss. However, it causes the problem of vanishing and exploding gradients, which makes the training of the GAN model unstable. In order to prevent this, Wasserstein distance based loss [2] is used. Mathematically, the training process of this conditional GAN using Wasserstein loss is formulated in the following way:

$$\begin{aligned} \min_G \max_D L_{GAN} = & \mathbb{E}_{\mathbf{x} \sim p_x(\mathbf{x})} [D(\mathbf{x})] \\ & - \mathbb{E}_{\mathbf{x}_u \sim p_{x_u}(\mathbf{x}_u)} [D(G(\mathbf{x}_u))], \end{aligned} \quad (13)$$

where  $p_x(\mathbf{x})$  is the distribution of the GT images, and  $p_{x_u}(\mathbf{x}_u)$  is the distribution of the aliased ZFR images.

In order to solve this optimization problem, an alternating process of updating  $G$  once and  $D$   $n_D$  times is followed. In order to enforce the Lipschitz constraint on  $D$ , weight clipping is applied on its weights [2].

### 2.4.2 Content Loss

Besides adversarial loss, other losses are required to bring the reconstructed output closer to the corresponding GT image. In order to do so, we incorporate an MAE based loss, so that the pixel-wise difference between the GT and the generated image is minimized. It is given by:

$$L_{\ell_1} = \mathbb{E}[\|G(\mathbf{x}_u) - \mathbf{x}\|_1], \quad (14)$$

where  $\|\cdot\|_1$  denotes the  $\ell_1$  norm. The  $\ell_1$  norm is preferred over the  $\ell_2$  norm which can lead to overly smooth and blurry reconstruction.

### 2.4.3 Structural Similarity Loss

As the high-frequency details in the MR image help in distinguishing various regions with structural information, it is extremely important to improve their reconstruction. SSIM quantifies the similarity between the local patches of two images on the basis of luminance, contrast and structure. It is calculated as follows:

$$SSIM(\mathbf{M}, \mathbf{N}) = \frac{2\mu_M\mu_N + \epsilon_1}{\mu_M^2 + \mu_N^2 + \epsilon_1} \frac{2\sigma_{MN} + \epsilon_2}{\sigma_M^2 + \sigma_N^2 + \epsilon_2}, \quad (15)$$

where  $\mathbf{M}$  and  $\mathbf{N}$  represent two image patches,  $\mu_M$  and  $\mu_N$  denote their means,  $\sigma_M^2$  and  $\sigma_N^2$  denote their variances,  $\sigma_{MN}$  denotes their covariance, and  $\epsilon_1, \epsilon_2$  are slack values to avoid division by zero.

In order to improve the perceptual quality of the reconstructed MR image and preserve the structural details, a mean SSIM (mSSIM) based loss is incorporated in the training of the generator. It maximizes the patch-wise SSIM between the reconstructed output and the corresponding GT image by minimizing the following expression:

$$L_{mSSIM} = 1 - \mathbb{E} \left[ \frac{1}{P} \sum_{p=1}^P SSIM(G_p(\mathbf{x}_u), \mathbf{x}_p) \right], \quad (16)$$

where  $P$  denotes the number of patches in the image.

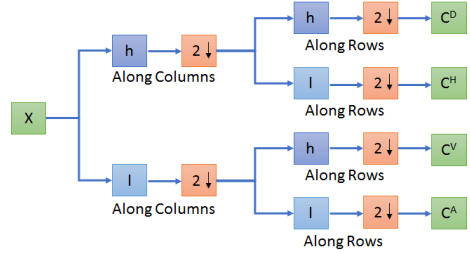


Figure 3. Illustration of the recursive process followed to compute the wavelet packet decomposition of  $\mathbf{X}$ . In this work, Haar wavelet is used, so that  $h = (\frac{1}{\sqrt{2}}, \frac{1}{\sqrt{2}})$  and  $l = (\frac{1}{\sqrt{2}}, \frac{-1}{\sqrt{2}})$ .

### 2.4.4 Wavelet Loss

In order to further enhance the textural details in the generated image, a weighted version of MAE in the wavelet domain is included as another loss term. This is inspired by another inverse problem which is closely related to CS-MRI reconstruction, namely super-resolution [20]. In order to decompose the image into sets of wavelet coefficients  $\mathbf{C}$ , which are equal in size, and correspond to even division of bands in the frequency domain, the wavelet packet transform is used. Fig. 3 depicts one step of the recursive process which is followed to obtain the sets of wavelet coefficients. For an  $r_w$  level decomposition which produces  $P_w = 4^{r_w}$  sets of wavelet coefficients of size  $K_w \times K_w$  with  $K_w = \frac{K}{\sqrt{P_w}}$ , the wavelet loss is formulated as follows:

$$L_{wvt} = \frac{1}{P_w K_w^2} \sum_{p=1}^{P_w} \gamma_p \left[ \sum_{i,j=1}^{K_w} |\mathbf{C}_{G(\mathbf{x}_u)}^p(i,j) - \mathbf{C}_{\mathbf{x}}^p(i,j)| \right],$$

where  $\gamma_p$  denotes the weight of the  $p^{th}$  set of coefficients. Since the pixel-wise MAE loss contributes more towards the improvement of low-frequency details, and the mSSIM loss focuses more on preserving the high-frequency content

Table 1. Quantitative results for ablation study of the proposed model

Network Settings	1 <sup>st</sup>	2 <sup>nd</sup>	3 <sup>rd</sup>	4 <sup>th</sup>	5 <sup>th</sup>	6 <sup>th</sup>
Complex-valued GAN	✗	✓	✓	✓	✓	✗
RRDBs	✗	✗	✓	✓	✓	✓
Dense U-net	✗	✗	✗	✓	✓	✓
Wavelet loss	✗	✗	✗	✗	✓	✓
Generator parameters	2M	1.2M	1.5M	1.7M	1.7M	3.5M
PSNR (dB) / mSSIM	39.640 / 0.9823	40.048 / 0.9866	41.418 / 0.9879	43.798 / 0.9902	<b>45.044 / 0.9919</b>	42.864 / 0.9858

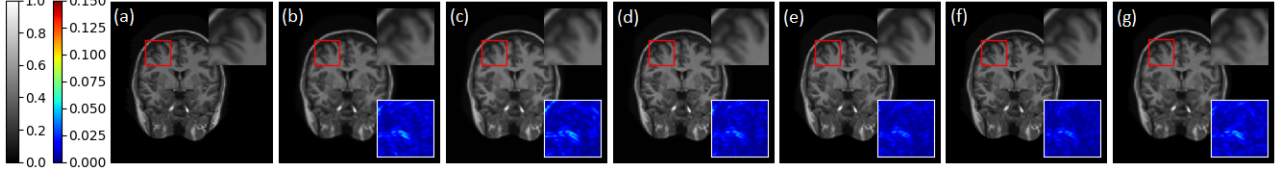


Figure 4. Qualitative results for ablation study of the proposed model. (a) GT, reconstruction results for (b) 1<sup>st</sup>, (c) 2<sup>nd</sup>, (d) 3<sup>rd</sup>, (e) 4<sup>th</sup>, (f) 5<sup>th</sup>, and (g) 6<sup>th</sup> network settings. Inset- top right: the zoomed in region enclosed by the red box, bottom right: absolute difference between the zoomed in region and its corresponding GT.

in the reconstructed image, higher weights  $\gamma_p$  are assigned to the wavelet coefficients corresponding to the band-pass components to improve their reconstruction. This is done by setting the weights according to the probability density function of a Gaussian distribution with mean  $\frac{(P_w-1)}{2}$  and variance  $\sigma_w^2$ . In this work,  $r_w = 3$ , i.e.  $P_w = 64$ , and  $\sigma_w^2 = 12.5$ .

#### 2.4.5 Overall Loss

The overall loss  $L$  which is used to train the generator, is formulated as a weighted sum of all the losses presented above:

$$L = \lambda_1 L_{GAN} + \lambda_2 L_{\ell_1} + \lambda_3 L_{mSSIM} + \lambda_4 L_{wvt}. \quad (17)$$

In this work,  $\lambda_1 = 0.01$ ,  $\lambda_2 = 20$ ,  $\lambda_3 = 1$ , and  $\lambda_4 = 100$ .

Once the training is complete, a single forward pass through the trained generator is used to obtain the reconstructed image.

#### 2.5. Training settings

For implementing the model, Keras framework with TensorFlow backend is used. The model is trained using 4 NVIDIA GeForce GTX 1080 Ti GPUs. In this work, the batch size is set as 16. In the generator, each layer produces 32 feature maps. A total of 4 RRDBs are present in the bottleneck layer, the number of dense blocks is set as 8, and  $\alpha$  is 0.2. The absolute value of the discriminator weights is clipped at 0.05, and  $n_D$  is set as 3. For training the model, we use Adam optimizer [24], with  $\beta_1 = 0.5$  and  $\beta_2 = 0.999$ . The initial LR is set as  $10^{-4}$ , with a decay of  $1.39 \times 10^{-3}$ , so that it becomes 1/10<sup>th</sup> of the initial value after 5 epochs.

### 3. Results and Discussion

#### 3.1. Dataset

We evaluate our models on T-1 weighted brain MR images taken from the MICCAI 2013 grand challenge dataset [26] as well as MR images of coronal view of knee from the MRNet dataset [4]. For the MICCAI 2013 dataset, 20787 images are used for training, after randomly choosing images from the train set, and then applying data augmentation with images containing 10% and 20% complex additive Gaussian noise in the Fourier space. For testing, 2000 images are selected at random from the test set provided in the dataset. For the MRNet dataset, 12500 images are randomly chosen for training with the same augmentation procedure, and 2000 non-overlapping images are chosen for testing.

#### 3.2. Ablation Studies

Table 1 and Fig. 4 show the quantitative and qualitative results, respectively, for ablation study of the model to showcase the importance of addition of various components in the proposed model. These results are reported for 30% 1D Gaussian (1D-G) undersampled images, from the MICCAI 2013 dataset. The first case demonstrates a real-valued GAN model comprised of a U-net based generator model without RRDBs, without the dense connections in the contracting and expanding paths, with CReLU activation and with  $\lambda_4 = 0$  in (17). In the next case, the complex-valued equivalent of the previous model is considered. In the third case, the effect of adding RRDBs in the last layer of the complex-valued U-net is observed without the wavelet loss. In the fourth case, the addition of dense connections in the complex-valued U-net is considered with the RRDBs, without the wavelet loss. In the fifth case, the effect of including

Table 2. Quantitative comparison of various activation functions

Activation	CReLU	CPReLU	$z$ ReLU	Cardioid	PP-SoS	TIP-SoS	PC-SoS
PSNR (dB) / mSSIM	45.044 / 0.9919	45.165 / 0.9920	35.991 / 0.9690	45.128 / 0.9919	45.066 / 0.9919	45.429 / 0.9925	<b>45.678 / 0.9927</b>

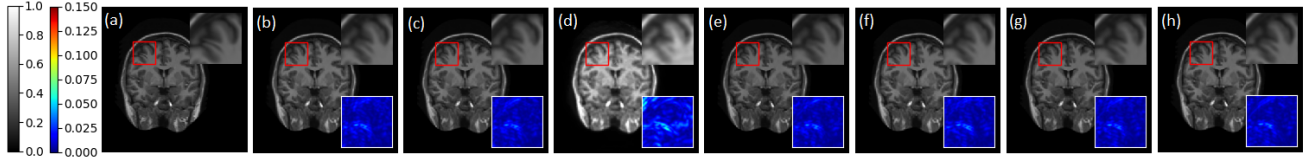


Figure 5. Qualitative comparison of various activation functions. (a) GT, reconstruction results using (b) CReLU, (c) CPReLU, (d)  $z$ ReLU, (e) Cardioid, (f) PP-SoS, (g) TIP-SoS, and (h) PC-SoS activation functions. Inset- top right: the zoomed in region enclosed by the red box, bottom right: absolute difference between the zoomed in region and its corresponding GT.

$L_{wvt}$  by setting  $\lambda_4 = 100$  is observed. Evidently, each step results in significant improvement in the quantitative metrics of peak signal-to-noise ratio (PSNR) and mSSIM, as well as in the qualitative reconstructions as demonstrated in Fig. 4. It can be observed that despite a 40% decrease in the number of generator parameters, the complex-valued equivalent (2<sup>nd</sup> setting) outperforms the real-valued GAN model presented as the 1<sup>st</sup> setting. In order to further highlight the importance of using complex-valued representations and their ability to produce high-quality reconstructions, the real-valued version of the fifth case of the ablation study is considered. In this model, each convolutional layer is converted from complex to real, but twice the number of output channels are present in each layer. The results for this model are shown in the last column of Table 1. It is observed that despite having more than twice the number of trainable parameters, this model significantly underperforms when compared to its complex-valued counterpart (5<sup>th</sup> setting). For the rest of the results, we use the 5<sup>th</sup> network settings.

### 3.3. Activation Functions

Table 2 and Fig. 5 show the quantitative and qualitative results for comparing various activation functions, respectively. These results are also reported for 30% 1D-G undersampled images, from the MICCAI 2013 dataset. It is observed that  $z$ ReLU, which only allows the inputs lying in the first quadrant to pass and blocks all other inputs, has the worst performance. CPReLU outperforms CReLU as well as  $z$ ReLU. This may be because unlike these activation functions, CPReLU does not suppress input information strongly for non-zero values of parameters  $\beta_R$  and  $\beta_I$ . Moreover, it has an adaptable shape which also allows it to bypass issues like dead neurons which CReLU can suffer from. It is also observed that PP-SoS obtains a similar performance as that of cardioid. However, these phase preserving activation functions underperform as compared to CPReLU, which does not have the phase preservation capabilities. Further, when the possibility of a negative gain is introduced in PP-SoS, the resulting activation TIP-SoS ob-

tains a significantly better performance. The same is true for the proposed PC-SoS, after the parameter  $\phi$  is introduced. This experiment not only highlights the superiority of PC-SoS, but also shows that phase preserving activation functions prove less effective in a complex GAN framework. Although all CPReLU, TIP-SoS and PC-SoS are not phase preserving activations, the superior performance of the latter two functions can be attributed to a higher flexibility in the resulting shape. The rest of the results are reported by using proposed PC-SoS activation, as it outperforms all the other activation functions by a considerable margin. This final model takes 37.87 ms to reconstruct each MR image. As the inference time is of the order of milliseconds, the proposed approach is viable for real-time reconstruction.

## 3.4. Comparison with State-of-the-art

### 3.4.1 MICCAI 2013 Dataset

Fig. 6 demonstrates the qualitative results of our final model and comparison with state-of-the-art (SOTA) methods for reconstruction of 30% 1D-G undersampled images. It is observed that the proposed model is able to reconstruct high-quality images by preserving most of the structural details of critical importance. As seen in the first row, some of the methods like FBPCNet, DLMRI, and BM3D are unable to properly reconstruct the high-frequency content present in the form of the edges in the zoomed in region. Also, most of the SOTA methods obtain blurry reconstruction results which might be due to the use of  $l_2$  loss by most of the methods. This can be clearly seen by the quality of reconstruction of the fine details present in the zoomed in region of the second image. FBPCNet, DLMRI, DeepADMM, and BM3D obtain an overly smooth low-quality reconstruction, which appears to be slightly out of focus. Moreover, one can also observe the presence of subtle artefacts in the background of the zoomed in region of the first image. On close inspection, it can be observed that FBPCNet, DLMRI, DeepADMM produce outputs with aliasing artefacts. The reconstructed images produced by DAGAN, although significantly better than other methods, do not capture subtle

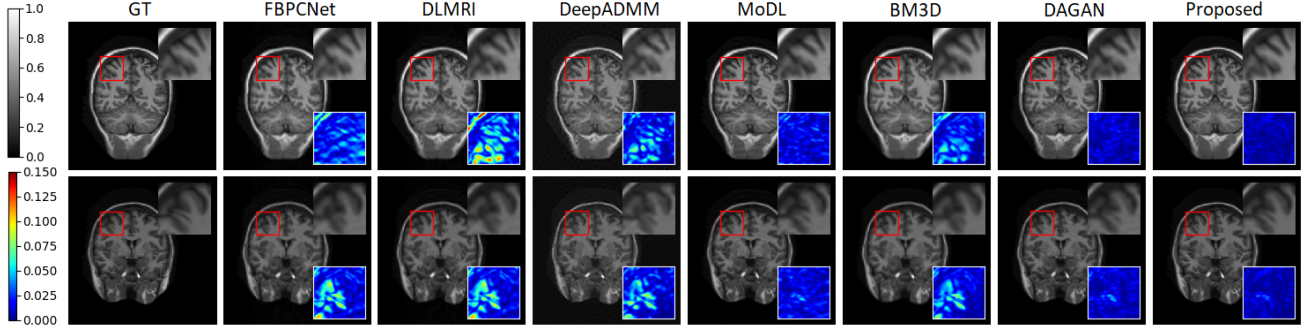


Figure 6. Qualitative results and comparison of the proposed method for two images taken from the MICCAI 2013 dataset. Inset- top right: the zoomed in region enclosed by the red box, bottom right: absolute difference between the zoomed in region and its corresponding GT.

details. The visual representations of the proposed scheme show that it preserves the fine structural and textural details and most closely aligns with the GT, as compared to the aforementioned SOTA methods. The difference between the reconstructed image and the GT supports the same.

Table 3. Quantitative comparison with previous methods using MICCAI 2013 dataset

Method	Noise-free images		10% noise level		20% noise level	
	PSNR (dB)	mSSIM	PSNR (dB)	mSSIM	PSNR (dB)	mSSIM
FBPCNet[23]	35.996	0.8655	34.025	0.6011	31.421	0.4226
DLMRI[35]	37.405	0.8732	34.144	0.6140	31.564	0.4346
DeepADMM[46]	41.545	0.8946	39.078	0.8105	35.373	0.6000
MoDL[1]	42.383	0.9760	40.204	0.9481	36.844	0.8572
BM3D[12]	42.521	0.9764	37.836	0.7317	33.657	0.4947
DAGAN[45]	43.329	0.9860	<b>42.006</b>	0.9814	<b>39.160</b>	0.9619
Proposed	<b>45.678</b>	<b>0.9927</b>	41.809	<b>0.9838</b>	39.083	<b>0.9718</b>

Table 3 illustrates the quantitative comparison of the proposed method with the six SOTA approaches. These results are reported for 30% 1D-G undersampled images. It can be observed that there is an appreciable boost in both PSNR and mSSIM values obtained by the proposed approach as compared to the existing approaches. On comparing the results for images with 10% and 20% noise, it is observed that some of the methods like FBPCNet, DLMRI, and BM3D experience a steep decline in the reconstruction quality with the addition of noise indicating a lack of robustness. The use of the augmentation technique with noisy images while preparing the training data for the proposed method increases its robustness towards noise. The values obtained by the proposed method for noisy images are significantly better than the other methods, but they are comparable to DAGAN. The reason for this might be the high complexity of the model, which allows superior reconstruction quality in the noise-free case at the cost of an increase in the sensitivity to the noise-level [38].

### 3.4.2 MRNet Dataset

To further analyze the effectiveness of the proposed method compared to DAGAN, we perform another set of experiments using the MRNet dataset. Table 4 and Fig. 7 show the

quantitative and qualitative results of the proposed method using 30% 1D-G undersampled images. It is observed that the proposed method significantly outperforms DAGAN for noise-free as well as noisy images. The proposed method obtains better PSNR and mSSIM results for images with 20% noise as compared to those obtained by DAGAN for noise-free images. The values of the metrics are in a lower range as compared to those in Table 3. This could be due to the higher content present in these images, as compared to those of MICCAI 2013 dataset, where the dark plain background occupies a larger portion of the image. The qualitative results as well the difference between the reconstructed output and the GT also demonstrate that the proposed method obtains superior reconstruction results.

Table 4. Quantitative results and comparison using MRNet dataset

Method	Noise-free images		10% noise level		20% noise level	
	PSNR (dB)	mSSIM	PSNR (dB)	mSSIM	PSNR (dB)	mSSIM
DAGAN[45]	31.529	0.8754	30.452	0.8182	28.267	0.7098
Proposed	<b>34.010</b>	<b>0.9306</b>	<b>33.031</b>	<b>0.9097</b>	<b>31.670</b>	<b>0.8802</b>

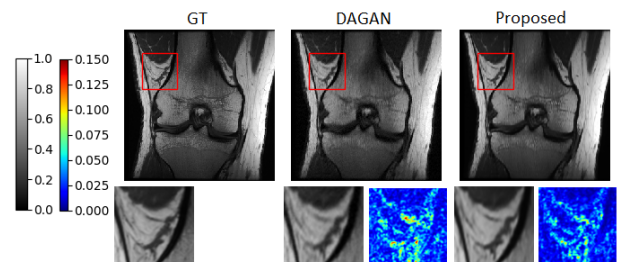


Figure 7. Qualitative result and comparison of the proposed method with DAGAN on images obtained from the MRNet dataset. Inset- bottom left: the zoomed in region enclosed by the red box, bottom right: absolute difference between the zoomed in region and its corresponding GT.

## 3.5. Effect of Sampling Masks

### 3.5.1 Sampling Ratio

Table 5 and Fig. 8 show the quantitative and qualitative results for comparing various sampling ratios, respectively.

These results are reported for 1D-G undersampled images, from the MICCAI 2013 dataset. It is observed the proposed approach is able to obtain high-quality reconstructions for both 20% and 30% undersampled images. The results obtained for 20% undersampled images are better than the results obtained by some of the SOTA methods for 30% undersampled images. For 10% undersampled images, the proposed approach is able to obtain a de-aliased output in which the contrast as well as some structural content has been preserved. However, it is evident that a highly faithful reconstruction may not be achieved for this ratio. This is because, the  $k$ -space has been highly undersampled, and only 10% of the data has been retained.

Table 5. Quantitative comparison of various sampling ratios

Sampling Ratio	10%	20%	30%
PSNR (dB) / mSSIM	35.799 / 0.9485	41.396 / 0.9817	45.678 / 0.9927

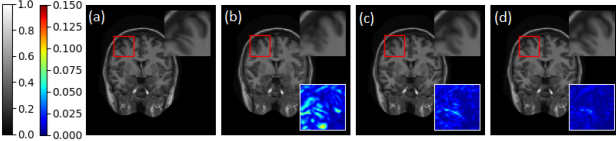


Figure 8. Qualitative comparison of various sampling ratios. (a) GT, reconstruction results of the proposed model using (b) 10%, (c) 20%, and (d) 30% sampling ratios. Inset- top right: the zoomed in region enclosed by the red box, bottom right: absolute difference between the zoomed in region and its corresponding GT.

Table 6. Quantitative comparison of various sampling patterns

Sampling Pattern	1D-G	Radial	Spiral
PSNR (dB) / mSSIM	45.678 / 0.9927	46.629 / 0.9922	46.747 / 0.9929

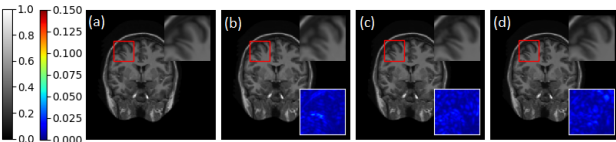


Figure 9. Qualitative comparison of various sampling patterns. (a) GT, reconstruction results of the proposed model using (b) 1D-G, (c) radial, and (d) spiral sampling patterns. Inset- top right: the zoomed in region enclosed by the red box, bottom right: absolute difference between the zoomed in region and its corresponding GT.

### 3.5.2 Sampling Pattern

Table 6 and Fig. 9 demonstrate the quantitative and qualitative results for comparing various sampling patterns, respectively. These results are reported for 30% undersampled images, from the MICCAI 2013 dataset. It is observed that all the three sampling patterns obtain high-quality reconstruction, as the difference between the generated output

and the GT is close to zero. The radial and spiral sampling patterns obtain even better reconstruction quality than the 1D-G pattern. This may be because unlike 1D-G, these patterns are more heavily concentrated towards the center as compared to the edges, which is also the case for the Fourier spectrum of MR images.

### 3.6. Zero-shot Inference

The model trained on 30% 1D-G undersampled brain images from the MICCAI 2013 dataset is tested for reconstruction of 30% 1D-G undersampled images of canine legs from the MICCAI 2013 challenge. This model achieves an average PSNR 42.949 dB and mSSIM 0.9864, when inferred for 2000 test images. The qualitative results of this zero-shot inference are presented in Fig. 10. It is observed that although the images of canine legs which are used for testing the model are completely different from those used during the training phase, it is able to obtain high-quality reconstruction.

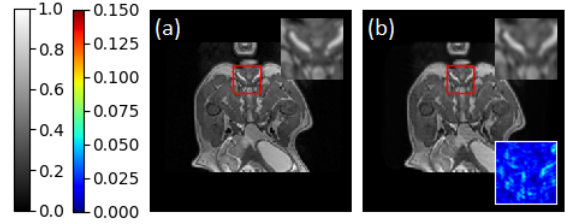


Figure 10. Qualitative results of zero-shot inference experiment. (a) GT, (b) reconstruction results of the proposed model trained on images from MICCAI 2013 dataset. Inset- top right: the zoomed in region enclosed by the red box, bottom right: absolute difference between the zoomed in region and its corresponding GT.

The proposed scheme using the  $L_{\ell_1}$ ,  $L_{mSSIM}$ ,  $L_{wvt}$  loss functions during training tries to align the reconstructed MR image closely to the GT, in effect trying to reduce the possibility of hallucination by GAN. All the aforementioned experiments, including the zero-shot inference, help demonstrate that the proposed Co-VeGAN framework has displayed no signs of hallucination.

## 4. Conclusion

In this paper, we introduced a novel Co-VeGAN framework, where a dense U-net based generator architecture is proposed, along with the use of pixel-wise  $\ell_1$  loss, a novel Gaussian-weighted wavelet loss, and an mSSIM based loss to ensure good reconstruction of the CS-MR images across the entire frequency range. The proposed activation function PC-SoS, which is not only sensitive to the input phase, but also a learnable function, further enhances the performance of the framework. Detailed analyses have shown that the proposed method significantly improves the quality of the reconstruction compared to SOTA CS-MRI reconstruction methods. The fast inference step opens up the possibil-

ity for a real-time implementation of the method, while the less number of generator parameters considerably reduces the storage requirement.

## References

- [1] H. K. Aggarwal, M. P. Mani, and M. Jacob. MoDL: Model-based deep learning architecture for inverse problems. *IEEE Transactions on Medical Imaging*, 38(2):394–405, 2019.
- [2] M. Arjovsky, S. Chintala, and L. Bottou. Wasserstein generative adversarial networks. In *International Conference on Machine Learning (ICML)*, volume 70, pages 214–223, 2017.
- [3] M. Arjovsky, A. Shah, and Y. Bengio. Unitary evolution recurrent neural networks. *ArXiv*, abs/1511.06464, 2015.
- [4] N. Bien et al. Deep-learning-assisted diagnosis for knee magnetic resonance imaging: Development and retrospective validation of MRNet. *PLoS Medicine*, 15, 2018.
- [5] A. Bora, A. Jalal, E. Price, and A. G. Dimakis. Compressed sensing using generative models. In *International Conference on Machine Learning (ICML)*, volume 70, pages 537–546, 2017.
- [6] S. Boyd, N. Parikh, E. Chu, B. Peleato, and J. Eckstein. Distributed optimization and statistical learning via the alternating direction method of multipliers. *Foundations and Trends in Machine Learning*, 3(1):1–122, 2011.
- [7] J. Bruna, S. Chintala, Y. LeCun, S. Piantino, A. Szlam, and M. Tygert. A mathematical motivation for complex-valued convolutional networks. *ArXiv*, abs/1503.03438, 2015.
- [8] I. Danihelka, G. Wayne, B. Uria, N. Kalchbrenner, and A. Graves. Associative long short-term memory. *ArXiv*, abs/1602.03032, 2016.
- [9] P. Deora, B. Vasudeva, S. Bhattacharya, and P. M. Pradhan. Robust compressive sensing MRI reconstruction using generative adversarial networks. *ArXiv*, abs/1910.06067, 2019.
- [10] C. Dong, C. C. Loy, K. He, and X. Tang. Image super-resolution using deep convolutional networks. *IEEE Transactions on Pattern Analysis and Machine Intelligence*, 38(2):295–307, 2016.
- [11] D. L. Donoho. Compressed sensing. *IEEE Transactions on Information Theory*, 52(4):1289–1306, 2006.
- [12] E. M. Eksioglu. Decoupled algorithm for MRI reconstruction using nonlocal block matching model: BM3D-MRI. *Journal of Mathematical Imaging and Vision*, 56(3):430–440, 2016.
- [13] I. Goodfellow et al. Generative adversarial nets. In *Advances in Neural Information Processing Systems 27*, pages 2672–2680. Curran Associates, Inc., 2014.
- [14] M. A. Griswold et al. Generalized autocalibrating partially parallel acquisitions (GRAPPA). *Magnetic Resonance in Medicine*, 47(6):1202–1210, 2002.
- [15] N. Guberman. On complex valued convolutional neural networks. *ArXiv*, abs/1602.09046, 2016.
- [16] Kerstin Hammernik et al. Learning a variational network for reconstruction of accelerated MRI data. *Magnetic Resonance in Medicine*, 79(6):3055–3071, 2018.
- [17] K. He, X. Zhang, S. Ren, and J. Sun. Delving deep into rectifiers: Surpassing human-level performance on imagenet classification. In *IEEE International Conference on Computer Vision (ICCV)*, pages 1026–1034, 2015.
- [18] A. Hirose and S. Yoshida. Generalization characteristics of complex-valued feedforward neural networks in relation to signal coherence. *IEEE Transactions on Neural Networks and learning systems*, 23(4):541–551, 2012.
- [19] G. Huang, Z. Liu, L. v. d. Maaten, and K. Q. Weinberger. Densely connected convolutional networks. In *IEEE Conference on Computer Vision and Pattern Recognition (CVPR)*, pages 2261–2269, 2017.
- [20] H. Huang, R. He, Z. Sun, and T. Tan. Wavelet-SRNet: A wavelet-based CNN for multi-scale face super resolution. In *IEEE International Conference on Computer Vision (ICCV)*, pages 1698–1706, 2017.
- [21] S. Ioffe and C. Szegedy. Batch normalization: Accelerating deep network training by reducing internal covariate shift. In *International Conference on Machine Learning (ICML)*, volume 37, pages 448–456. JMLR.org, 2015.
- [22] P. Isola, J. Zhu, T. Zhou, and A. A. Efros. Image-to-image translation with conditional adversarial networks. In *IEEE Conference on Computer Vision and Pattern Recognition (CVPR)*, pages 5967–5976, 2017.
- [23] K. H. Jin, M. T. McCann, E. Froustey, and M. Unser. Deep convolutional neural network for inverse problems in imaging. *IEEE Transactions on Image Processing*, 26(9):4509–4522, 2017.
- [24] D. P. Kingma and J. Ba. Adam: A method for stochastic optimization. In *International Conference on Learning Representations (ICLR)*, 2015.
- [25] K. Kreutz-Delgado. The complex gradient operator and the CR-calculus. *ArXiv*, abs/0906.4835, 2009.
- [26] B. Landman and S. Warfield (Eds.). 2013 Diencephalon standard challenge.
- [27] Y. Liu et al. Balanced sparse model for tight frames in compressed sensing magnetic resonance imaging. *PLOS ONE*, 10(4):1–19, 2015.
- [28] M. Lustig, D. Donoho, and J. M. Pauly. Sparse MRI: The application of compressed sensing for rapid MR imaging. *Magnetic Resonance in Medicine*, 58(6):1182–1195, 2007.
- [29] M. Mardani et al. Deep generative adversarial neural networks for compressive sensing MRI. *IEEE Transactions on Medical Imaging*, 38(1):167–179, 2019.
- [30] M. Mirza and S. Osindero. Conditional generative adversarial nets. *ArXiv*, abs/1411.1784, 2014.
- [31] T. Nitta. On the critical points of the complex-valued neural network. In *International Conference on Neural Information Processing (ICONIP)*, volume 3, pages 1099–1103, 2002.
- [32] A. V. Oppenheim and J. S. Lim. The importance of phase in signals. *Proceedings of the IEEE*, 69(5):529–541, 1981.
- [33] K. P. Pruessmann, M. Weiger, M. B. Scheidegger, and P. Boesiger. SENSE: Sensitivity encoding for fast MRI. *Magnetic Resonance in Medicine*, 42(5):952–962, 1999.
- [34] T. M. Quan, T. Nguyen-Duc, and W. Jeong. Compressed sensing MRI reconstruction using a generative adversarial network with a cyclic loss. *IEEE Transactions on Medical Imaging*, 37(6):1488–1497, 2018.

[35] S. Ravishankar and Y. Bresler. MR image reconstruction from highly undersampled k-space data by dictionary learning. *IEEE Transactions on Medical Imaging*, 30(5):1028–1041, 2011.

[36] D. P. Reichert and T. Serre. Neuronal synchrony in complex-valued deep networks. *ArXiv*, abs/1312.6115, 2013.

[37] O. Ronneberger, P. Fischer, and T. Brox. U-net: Convolutional networks for biomedical image segmentation. In *International Conference on Medical Image Computing and Computer-Assisted Intervention (MICCAI)*, pages 234–241. Springer, 2015.

[38] P. Roy, S. Ghosh, S. Bhattacharya, and U. Pal. Effects of degradations on deep neural network architectures. *ArXiv*, abs/1807.10108, 2018.

[39] C. Trabelsi et al. Deep complex networks. In *International Conference on Learning Representations (ICLR)*, 2018.

[40] P. Virtue, S. X. Yu, and M. Lustig. Better than real: Complex-valued neural nets for MRI fingerprinting. In *IEEE International Conference on Image Processing (ICIP)*, pages 3953–3957, 2017.

[41] Shanshan Wang et al. DeepcomplexMRI: Exploiting deep residual network for fast parallel MR imaging with complex convolution. *Magnetic Resonance Imaging*, 68:136 – 147, 2020.

[42] X. Wang et al. ESRGAN: Enhanced super-resolution generative adversarial networks. In *The European Conference on Computer Vision (ECCV) Workshops*, pages 63–79, 2018.

[43] S. Wisdom, T. Powers, J. Hershey, J. Le Roux, and L. Atlas. Full-capacity unitary recurrent neural networks. In *Advances in Neural Information Processing Systems*, pages 4880–4888, 2016.

[44] J. Xie, L. Xu, and E. Chen. Image denoising and inpainting with deep neural networks. In *Advances in Neural Information Processing Systems 25*, pages 341–349. Curran Associates, Inc., 2012.

[45] G. Yang et al. DAGAN: Deep de-aliasing generative adversarial networks for fast compressed sensing MRI reconstruction. *IEEE Transactions on Medical Imaging*, 37(6):1310–1321, 2018.

[46] Y. Yang, J. Sun, H. Li, and Z. Xu. Deep ADMM-Net for compressive sensing MRI. In *Advances in Neural Information Processing Systems 29*, pages 10–18. Curran Associates, Inc., 2016.

[47] Z. Wang, A. C. Bovik, H. R. Sheikh, and E. P. Simoncelli. Image quality assessment: From error visibility to structural similarity. *IEEE Transactions on Image Processing*, 13(4):600–612, 2004.

[48] Z. Zhang, H. Wang, F. Xu, and Y. Jin. Complex-valued convolutional neural network and its application in polarimetric SAR image classification. *IEEE Transactions on Geoscience and Remote Sensing*, 55(12):7177–7188, 2017.